Simulation of Deep Surge in a Turbocharger Compression System

Rick Dehner
Department of Mechanical and Aerospace Engineering,
The Ohio State University,
Columbus, OH 43210
e-mail: dehner.10@osu.edu

Ahmet Selamet
Department of Mechanical and Aerospace Engineering,
The Ohio State University,
Columbus, OH 43210
e-mail: selamet.1@osu.edu

Philip Keller
BorgWarner, Inc.,
Auburn Hills, MI 48326

Michael Becker
BorgWarner, Inc.,
Ludwigsburg 71636, Germany

Large-amplitude deep surge instabilities are studied in a turbocharger compression system with a one-dimensional (1D) engine simulation code. The system consists of an upstream compressor duct open to ambient, a centrifugal compressor, a downstream compressor duct, a large plenum, and a throttle valve exhausting to ambient. As the compressor mass flow rate is reduced below the peak pressure ratio for a given speed, mild surge oscillations occur at the Helmholtz resonance of the system, and a further reduction in flow rate results in deep surge considerably below the Helmholtz resonance. At the boundary with mild surge, the deep surge cycles exhibit, for the particular system considered, a long cycle period containing four distinct flow phases, including quiet (stable), instability growth (mild surge), blowdown (reversal), and recovery. Further reductions in flow rate decrease the deep surge cycle period, eliminate the quiet flow phase, and shorten the duration of the instability growth phase. Simulated oscillations of nondimensional flow rate, pressure, and speed parameters show good agreement with the experimental results available in literature, in terms of deep surge cycle flow phases along with the amplitude and frequency of the resulting fluctuations. The predictions illustrate that the quiet and instability growth phases, exhibited by this compression system, disappear as the plenum volume is substantially reduced. [DOI: 10.1115/1.4033260]

1 Introduction

The total-to-static pressure ratio $PR_{c,ts}$ versus mass flow rate $\dot{m}_c$ characteristics of centrifugal compressors are typically continuous, for a fixed rotational speed. Where the slope $dPR_{c,ts}/d\dot{m}_c$ of the compressor characteristic is negative, the pressure ratio of the compressor increases in a stable mode as the mass flow rate is reduced, as shown in Fig. 1. The slope becomes positive at low mass flow rates due to the presence of a "progressive stall" [1]. When the compressor operates along this positively sloped portion of its characteristic, the compression system is susceptible to surge instabilities. The stall in centrifugal compressors manifests itself in different modes, including (1) full- and part-span rotating stall; (2) axisymmetric stall near the inducer tips; and (3) stationary nonaxisymmetric stall produced by downstream asymmetry of the volute [1]. Stalling is often tolerated in centrifugal compressors without a drastic decrease in performance since the majority of pressure rise is attributed to the centrifugal effects.

The centrifugal compressor in this study operates on a turbocharger test bench between two circular ducts, with the inlet duct open to ambient and the exit duct connected to a plenum of larger cross-sectional flow area, as shown in Fig. 2 [2]. The plenum in the present study has an unusually large volume of $V_p = 208$ L, in order to demonstrate the effect of plenum size on the location of the surge line and obtain a low surge frequency [3]. The flow exiting the plenum then passes through a restriction (throttle) with a cross-sectional area considerably smaller than the plenum. The compression system in Fig. 2 has some resemblance to induction systems of turbocharged internal combustion engines. The intercooler and/or intake manifold volume along with the throttle and/or intake valve restriction may be represented by the plenum and throttle, respectively. The numbered locations (0–8) in Fig. 2 are utilized to denote locations throughout the compression system in the following discussions.

Surge is a self-excited system instability, and the occurrence of surge is dependent upon both the local slope (Fig. 1) of the compressor characteristic and the ducting (Fig. 2) in which the compressor is installed. Surge involves axisymmetric oscillations of pressure and mass flow rate, which can be categorized as "mild" or "deep" depending on the degree of mass flow fluctuation. "Mild surge" represents the conditions where the annulus average mass flow oscillates but remains in the forward direction at all times. Such oscillations are characterized by the Helmholtz frequency

$$f_H = \frac{a_p}{2\pi}\sqrt{\frac{A_C}{V_p L_C}}\left(\tag{1}$$

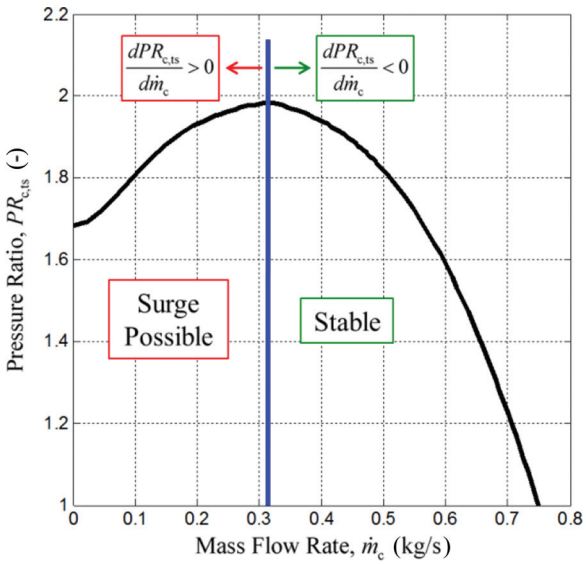

Fig. 1 Compressor characteristic exhibiting progressive stall

Contributed by the International Gas Turbine Institute (IGTI) of ASME for publication in the JOURNAL OF TURBOMACHINERY. Manuscript received January 15, 2016; final manuscript received February 29, 2016; published online May 10, 2016. Editor: Kenneth C. Hall.

 Copyright © 2016 by ASME

Downloaded From: http://turbomachinery.asmedigitalcollection.asme.org/ on 05/10/2016 Terms of Use: http://www.asme.org/about-asme/terms-of-use

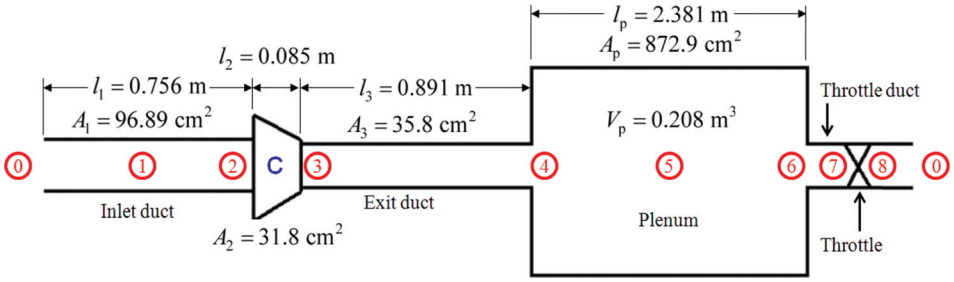

Fig. 2 Large *B* compression system of Fink [2]

of the compression system [3], where a_p is the speed of sound in the plenum, V_p is the volume of compressed air, A_C is the equivalent cross-sectional compressor duct area (inducer eye area), and L_C is the equivalent length of the duct. If the mass flow oscillations are severe and the mean flow reverses its direction during part of the cycle, the compressor has entered "deep surge" which can be detrimental to both the turbocharger and engine. The dominant deep surge frequency is below the Helmholtz resonance of the compression system. One manifestation of surge is discrete low frequency sound peaks.

Zero-dimensional (lumped parameter) models have been developed to predict the surge behavior of both axial [4] and centrifugal [5] compression systems with reasonable accuracy. These models formulated a set of nonlinear equations to estimate the system dynamics for the compression system configuration in Fig. 2. Greitzer's approach [4] has been used extensively in literature to estimate the operating point for surge inception and the subsequent oscillations. This analysis has revealed a dimensionless number defined by

$$B = \frac{U}{2a_p}\sqrt{\frac{V_p}{A_C L_C}} \tag{2}$$

where U is the impeller blade tip speed. Greitzer has suggested that, above a critical value of B, surge becomes the instability mode encountered. Hence, the onset of surge is a function of the impeller blade tip Mach number as well as the geometry of the compression system. The stall/surge boundary in Greitzer's work was measured and predicted to occur at B values around 0.8 [6] and 0.7 [5], respectively. Such specific values, however, cannot be generalized to all compressors. For example, measurements demonstrating the occurrence of both mild and deep surge in a centrifugal compression system with $B = 0.38$ were recently presented by Uhlenhake et al. [7]. This recent study confirmed that reducing B allowed the compressor to operate free of deep surge at lower mass flows, however, a low B did not guarantee that the compression system would operate surge-free when the compressor mass flow was further decreased. Hansen et al. [8] demonstrated that Greitzer's model could be extended to centrifugal compressors. The approach was further advanced by Fink [2] to include the shaft speed dynamics for a surging centrifugal compressor as an integral part of the cycle. A method for implementing the foregoing lumped model into a zero-dimensional engine simulation code has been outlined by Theotokatos and Kyrtatos [9]. They simulated the mild and deep surge experimental operating conditions presented by Fink et al. [3], providing reasonable agreement with measurements. An unsteady, 1D, time-domain approach was used by Dehner et al. [10] to simulate the mild surge experimental results presented by Fink [2,3], providing good agreement.

Fink [2,3] studied a turbocharger for diesel applications. The compressor was radial with 20 main blades (no splitters) and utilized a vaneless diffuser. The impeller had a tip diameter of 12.8 cm, a rotational inertia of 0.001 kg m^2, and was designed to operate at rotational speeds up to $N = 70{,}000$ rpm (70 krpm). The experimentally determined compressor characteristics were presented as total-to-total pressure ratio $PR_{c,tt}$ versus corrected mass flow rate $\dot{m}_{c,cor}$ at constant, corrected rotational speeds of 25, 33, 39, 45, 48, and 51 krpm for both a large and small B compression system, as shown in Fig. 3. The rotational speed is corrected for total compressor inlet temperature T_{02} as

$$N_{cor} = \frac{N}{\sqrt{T_{02}/T_{ref}}} \tag{3}$$

where $T_{ref} = 298$ K, the standard reference temperature. The compressor mass flow rate $\dot{m}_c$ is corrected for T_{02} and total compressor inlet pressure p_{02} as

$$\dot{m}_{c,cor} = \dot{m}_c \frac{\sqrt{T_{02}/T_{ref}}}{p_{02}/p_{ref}} \tag{4}$$

where $p_{ref} = 100$ kPa, the standard reference pressure. Fink's large B system was designed with a large plenum (208 L) such that $B = 2.74$ at $N = 48$ krpm and surge was the instability mode encountered at low mass flow rates. When the compressor mass flow rate was reduced at $N = 48$ krpm, the large B system entered mild surge as the slope of the characteristic became positive and deep surge was initiated as the flow rate was further decreased. The "Large B Surge Line," in Fig. 3, designates the mild/deep surge boundary for this system. While operating in deep surge at

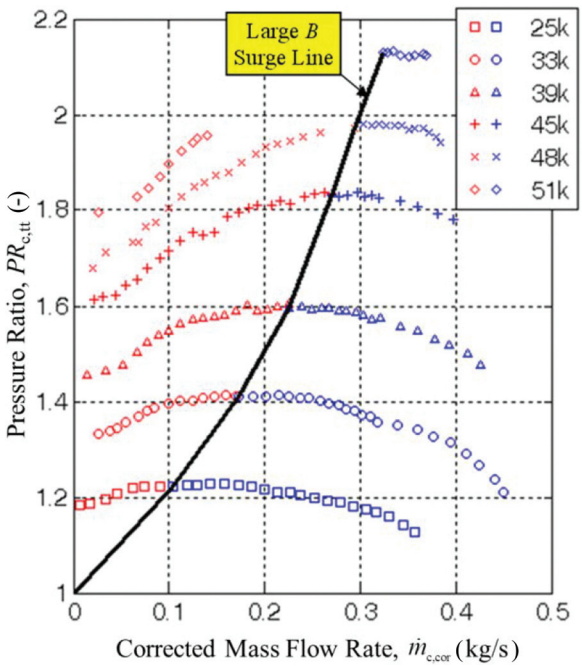

Fig. 3 Fink's small (red symbols) and large (blue symbols) *B* compressor characteristics

Downloaded From: http://turbomachinery.asmedigitalcollection.asme.org/ on 05/10/2016 Terms of Use: http://www.asme.org/about-asme/terms-of-use

the border with mild surge, the compressor surge cycles consist of four distinct flow phases, including quiet (stable), instability growth (mild surge), blowdown (flow reversal), and recovery. As the time-averaged compressor flow rate was further reduced (by reducing the throttle flow area) the quiet period was eliminated from the deep surge cycles and the duration of the instability growth phase decreased.

The small *B* compression system minimized the volume of compressed air by eliminating the plenum and placed the throttle valve just downstream of the compressor exit, giving $B = 0.25$ (at $N = 48$ krpm). This small *B* system was capable of operating without deep surge [3] at mass flow rates significantly lower than that of the large *B* system, as shown in Fig. 3. To the right of the Large *B* Surge Line, the characteristics are identical, indicating that the compressor characteristics are independent of the compression system ducting (a property of the compressor alone), yet the coupled compression system (compressor, ducting, and throttle) dictates the stable portion of the map available for use (location of the surge line).

Mild surge simulation results were presented by Dehner et al. [10], which showed good agreement with the experimental results of Fink [2,3], in terms of time-averaged operating point along with the amplitude and frequency of oscillations. The study developed a compressor map preprocessor to extrapolate and interpolate the compressor data to cover the entire forward flow operating region. This map was input to a 1D model of Fink's large *B* compression system ducting in order to provide the necessary compressor performance information. Incorporating the surge prediction capability into 1D code allowed many of the simplifying assumptions of the lumped analyses to be eliminated, and improved the agreement of simulations with experiments. In addition, a detailed analysis of the fluctuating pressure, temperature, and mass flow rate was provided at key compression system locations.

The objective of the present study is to reproduce the unsteady *deep* surge physics observed experimentally by Fink [2,3], using a 1D time-domain approach. The large *B* compression system ducting from the turbocharger test bench of Fink is modeled using a commercially available engine simulation code [11]. A schematic of the compression system geometry is shown in Fig. 2. The steady-state compressor data (recall Fig. 3) is preprocessed using a MATLAB script and incorporated into the model as a text file which provides the compressor performance information. This investigation focuses on predicting the compressor deep surge flow phases (quiet, instability growth, blowdown, and recovery) along with the amplitude and frequency of the resulting oscillations.

Following this introduction, Sec. 2 describes the compressor map and the 1D compression system model. Simulation results from the present study are then compared with the experimental observations of Fink [2] in Sec. 3. Section 4 provides insight into the factors contributing to the occurrence of the unusual quiet and instability growth deep surge flow phases exhibited by this compression system. Finally, concluding remarks are presented in Sec. 5.

2 Compression System Model

The compression system surge was modeled by incorporating a number of significant modifications to the compressor characterization of a commercially available, quasi 1D engine simulation code [11]. The ducting (compressor inlet, compressor outlet, plenum, and throttle ducts) geometry of the large *B* turbocharger bench compression system is defined in the model by connecting straight, circular cross section pipes with the exact dimensions of the experimental setup [2]. These ducts are discretized into control volumes which are 40 mm in length, and the code solves the nonlinear balance equations of mass, momentum, and energy in the time domain for each cell. The upstream opening of the compressor inlet duct and the downstream opening of the throttle duct are connected to identical temperature and pressure boundary conditions of 298 K and 1 bar, respectively. The throttle (valve) restriction is modeled as a circular orifice, and the diameter is adjusted to change the compressor operating point. Section 3 compares predictions to experimental deep surge data at four different compressor operating points, and a change in orifice (throttle) diameter is the primary factor among the provided prediction results (except when explicitly stated in Sec. 3.4). Identical to the experimental method of Fink [2], the turbine drive torque of the model was also reduced for the shorter duration (1.22 and 0.68 s) deep surge cycles, in order to maintain a constant time-averaged rotational speed.

The compressor portion of the model consists of a 0D table (actuator disk) providing the steady-state compressor performance, along with two additional ducts representative of the key geometrical features of the compressor. The first of these "equivalent compressor geometry" ducts represents the geometry of the compressor from the inlet duct connection to the impeller outlet, and it is positioned between the compressor inlet duct and the actuator disk. The second duct, positioned between the actuator disk and the compressor outlet duct, represents the geometry of the diffuser and volute. Both equivalent compressor geometry ducts are straight with circular cross sections, and their dimensions (diameter and length) are defined to preserve the length of the mean flow path and volume of the compressor. By including the key geometrical dimensions (length and volume) of the compressor, the predictions are improved during unsteady operation because the distance for pressure wave propagation and volume for mass storage are preserved.

The actuator disk portion of the compressor model is based on the steady-state performance data (recall Fig. 3) from both the small and large *B* systems of Fink. A compressor map preprocessor [10,12,13] was developed to extrapolate constant, corrected speed experimental data to choke ($PR = 1$), zero mass flow rate, reverse flow, and to zero speed. The positively sloped portion of the compressor constant speed lines is critical to properly predict compression system surge, and this region is well defined by the extended low-flow range experimental data from the small *B* compression system. This low-flow data was extrapolated to zero mass flow rate by utilizing the radial equilibrium theory and assuming an isentropic process [9] to approximate the pressure ratio as

$$PR_0 = C_{PR}\left[1 + \frac{\gamma - 1}{2\gamma R T_2}\omega^2 \left(r_2^2 - r_1^2\right)\right]^{\frac{\gamma}{\gamma - 1}} \tag{5}$$

where C_{PR} is a constant multiplier, γ is the ratio of specific heats, R is the gas constant for air, T_2 is the compressor inlet temperature, ω is the angular velocity of the impeller, r_2 is the radius of the exducer tip, and

$$r_1 = \sqrt{\frac{r_{1,t}^2 + r_{1,h}^2}{2}} \tag{6}$$

is the mean geometric radius of the impeller eye, which divides the impeller eye area into two sections of equal area, with $r_{1,t}$ and $r_{1,h}$ being the radii of the inducer tip and hub, respectively. For the present study, a C_{PR} value slightly larger than unity was applied to PR_0 in Eq. (5) to better match the experimental data, as shown in Fig. 4. This multiplier was 1.04 for the lowest speed (25 krpm) and 1.09 for the highest compressor speed (51 krpm). The pressure ratio versus flow rate characteristics were estimated in the reverse flow operating region by a quadratic function [7], which is defined such that it is continuous with the forward flow data with zero slope at the intercept ($\dot{m} = 0$). Additional information regarding extrapolation and interpolation within the forward flow region of the compressor was previously provided [10], so the remainder of the present description will primarily focus on steady-state compressor performance during flow reversal.

Downloaded From: http://turbomachinery.asmedigitalcollection.asme.org/ on 05/10/2016 Terms of Use: http://www.asme.org/about-asme/terms-of-use

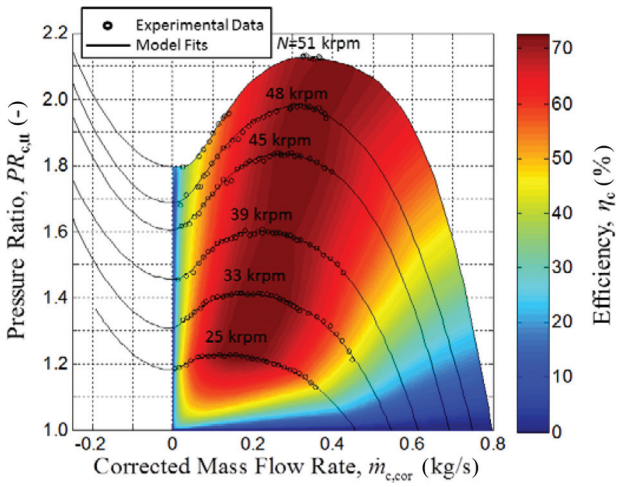

Fig. 4 Map of Fink's [2] compressor used for the model

The compressor efficiency and power are used interchangeably to define the temperature change through the compressor and the rate of shaft work, since adiabatic operation is assumed for the compressor. During forward flow, the more familiar isentropic efficiency is utilized, as shown in Fig. 4, and compressor power is preferred within the reverse flow region, as shown in Fig. 5, since the standard definition of efficiency becomes negative (even though the compressor is still doing work on the air). The reverse flow compressor power is approximated from the forward flow nondimensional torque

$$\Gamma_c = \frac{\tau_c}{\rho_0 A_c r_2 U^2} = \frac{\dfrac{\dot{m}_c c_p T_{02}}{\omega \eta_{c,tt}} PR_{c,tt}^{\frac{\gamma-1}{\gamma}} - 1}{\rho_0 A_c r_2 U^2} \tag{7}$$

where τ_c is the torque driving the compressor, ρ_0 is the density of air at ambient conditions, c_p is specific heat of air at constant pressure, T_{02} is the total inlet temperature, and $\eta_{c,tt}$ is the total-to-total isentropic efficiency of the compressor. When the nondimensional torque is plotted against compressor flow coefficient (nondimensional mass flow rate)

$$\phi_c = \frac{C_{x,2}}{U} = \frac{\dot{m}_c}{\rho_2 A_C U} \tag{8}$$

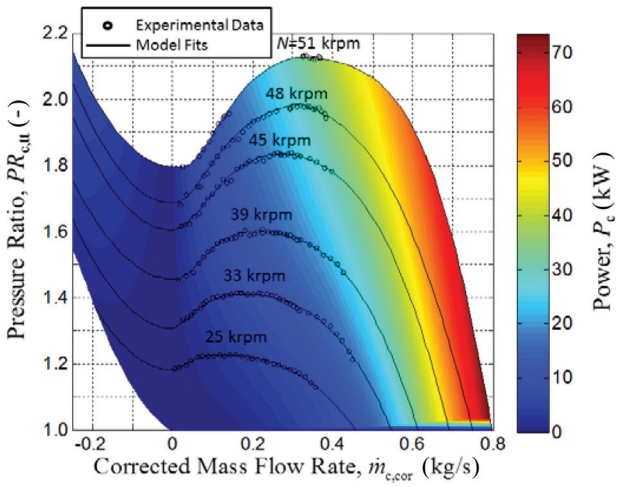

Fig. 5 Power absorbed by the compressor of Fink [2]

the data at all rotational speeds nearly collapses on a single curve, where $C_{x,2}$ and ρ_2 are the axial velocity and density at the compressor inlet, respectively. The Γ_c versus ϕ_c data provides a convenient means for extrapolating compressor isentropic efficiency to zero mass flow rate by applying a quadratic fit that intersects the intercept ($\phi_c = 0$) at $\Gamma_c = 0$, and the nondimensional torque during reverse flow is estimated from the forward fits as a fraction (0.16 here) of the mirror image over $\phi_c = 0$ (refer to Ref. [13] for further details).

In order to incorporate nonzero compressor power during flow reversal, the current study applies a power to the turbocharger shaft. The magnitude of the applied power is determined as a function of the corrected mass flow rate and pressure ratio by means of a lookup table utilizing data from the reverse flow portion of Fig. 5. The energy which is transferred from the impeller to the air during reverse flow is accounted for as a source term, which is applied to the energy conservation equation for the first control volume in the equivalent compressor exit duct neighboring the compressor (refer to Ref. [12] for additional details).

After the preprocessor extrapolates the experimental data to cover the entire forward and reverse flow operating range, it interpolates the data at intermediate rotational speeds and writes the information to a file with the correct format to be used directly by the 0D compressor object (actuator disk) of the engine simulation code.

3 Deep Surge Simulation Results

The simulations in the current study are aimed at reproducing the experimental deep surge observations from Fink's [2,3] large *B* compression system. Fink presents his experimental surge results at a time-averaged, corrected rotational speed of 48 krpm ($Ma_{t,0} = 0.92$). During mild surge, the ϕ_c data fluctuates about a time mean value of 0.23 with an amplitude of 20% of the mean flow, and the dominant frequency of oscillations is reported as 7.3 Hz. Starting at this mild surge operating point, a slight reduction in flow rate produced deep surge with a cycle period of $T_{DS} = 3.6$ s, including quiet, instability growth, blowdown, and recovery flow phases, as shown in Fig. 6. The flow coefficient in Fig. 6 is based on velocity measurements from a hotwire anemometer, which is insensitive to flow direction. In order to distinguish between forward and reverse flow, Fink applied a mass balance to the plenum volume to estimate the compressor mass flow rate and therefore flow coefficient. The flow coefficient derived from the plenum mass balance in Fig. 6 confirms that the flow is indeed reversed during the blowdown phase. Fink provided results from the plenum mass balance to differentiate the flow direction in the time domain only for the $T_{DS} = 3.6$ s case in Fig. 6, making it the single reverse flow experimental result in the time domain to compare with predictions. A simulated ϕ_c from the present study, with $T_{DS} = 3.6$ s, is presented in Fig. 7 and exhibits a reasonable agreement with the experimental results in Fig. 6. The minimum ϕ_c is predicted as 0.158, which appears to agree closely with that estimated by applying the plenum mass balance to measurements. During the recovery phase, the maximum ϕ_c is predicted to reach 0.383, which lies between the hotwire and plenum mass balance values from the measurement. During the quiet and instability growth phases, the estimated compressor flow coefficient from the plenum mass balance is nearly identical to that obtained from the hotwire velocity measurement, as shown in Fig. 6. However, the maximum hotwire measurement during the recovery phase is lower than the plenum mass balance estimation.

The experimental observations of Fink [2] demonstrated that T_{DS} decreased and the flat "quiet" period in Fig. 6 was eliminated as the throttle flow area (rate) was further reduced. He presented three deep surge operating points with $T_{DS} = 3.0$, 1.24, and 0.70 s, including time-resolved fluctuations of ϕ_c along with two additional nondimensional parameters (impeller exit tip Mach Number $Ma_{t,0}$ and plenum isentropic head coefficient ψ_p). The plenum isentropic head coefficient is defined as

Downloaded From: http://turbomachinery.asmedigitalcollection.asme.org/ on 05/10/2016 Terms of Use: http://www.asme.org/about-asme/terms-of-use

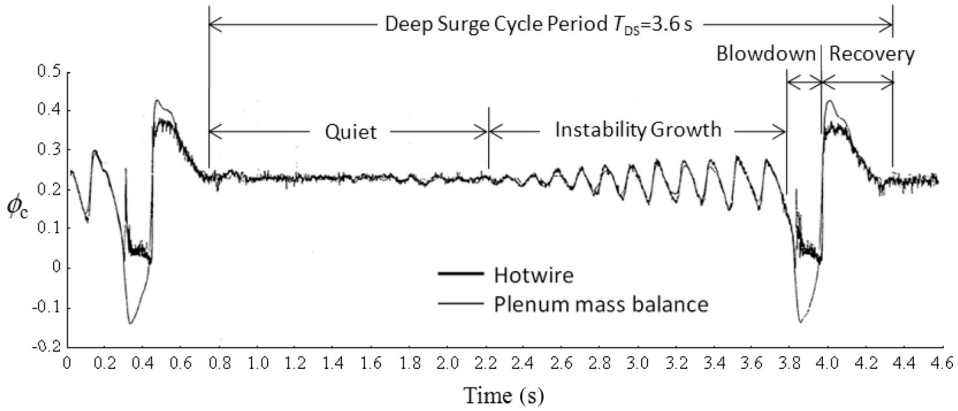

Fig. 6 Compressor flow coefficient calculated from the hotwire velocity measurement and plenum mass balance with $T_{DS} = 3.6$ s, from Fink [2]

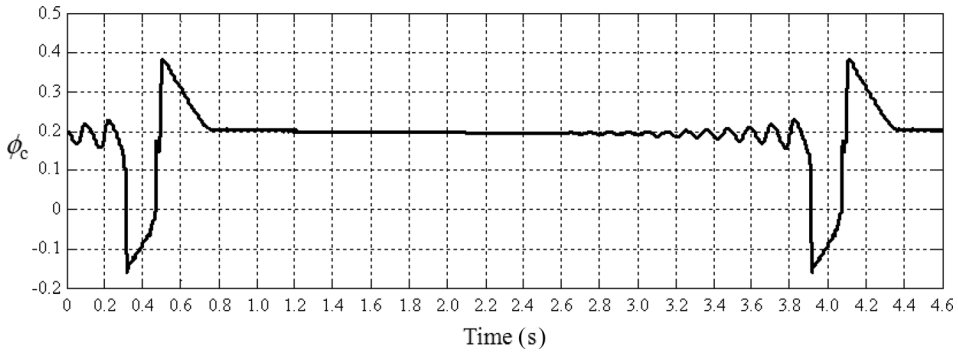

Fig. 7 Predicted compressor flow coefficient with $T_{DS} = 3.6$ s

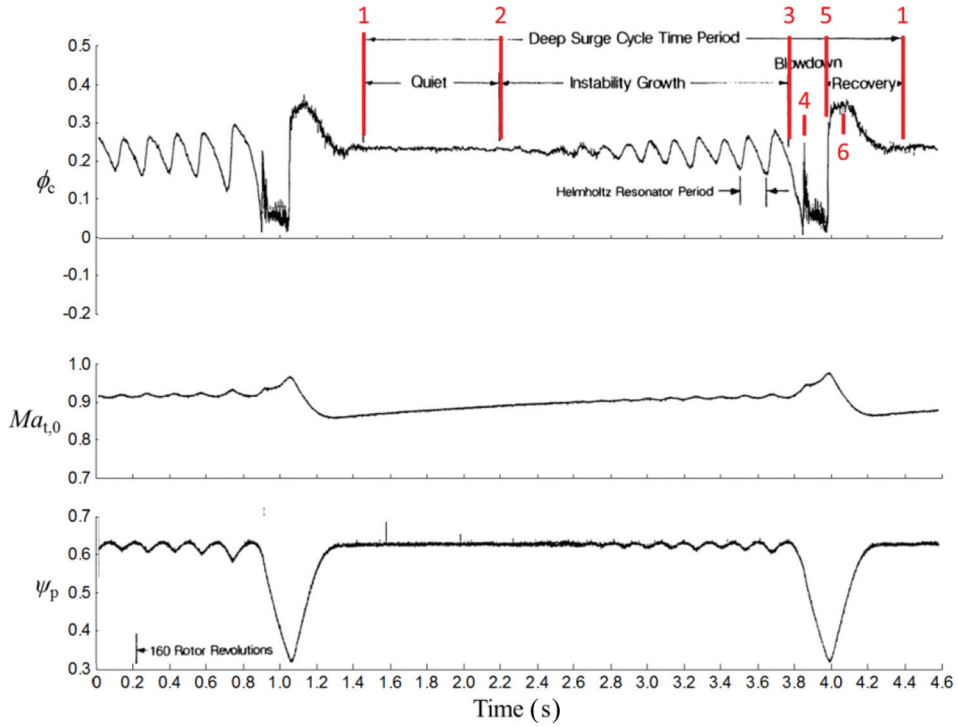

Fig. 8 Deep surge experimental data of Fink [2] with $T_{DS} = 3.0$ s

Downloaded From: http://turbomachinery.asmedigitalcollection.asme.org/ on 05/10/2016 Terms of Use: http://www.asme.org/about-asme/terms-of-use

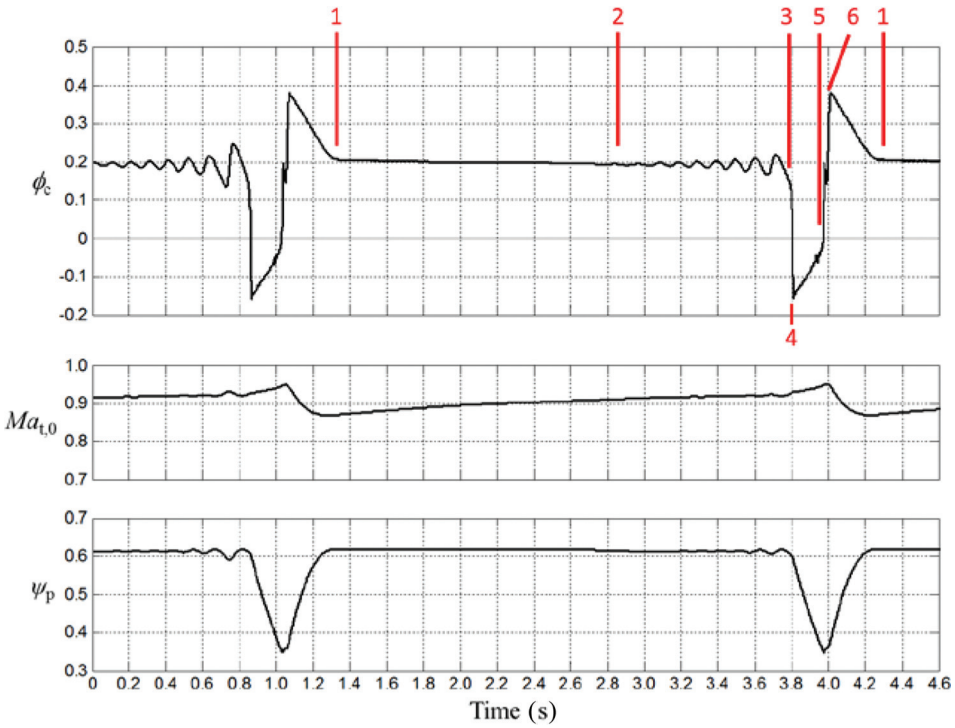

Fig. 9 Deep surge prediction with $T_{DS} = 3.0$ s

$$\psi_p = \frac{\Pi_p^{(\gamma-1)/\gamma} - 1}{(\gamma - 1)Ma_{t,0}^2} \tag{9}$$

where

$$\Pi_p = \frac{p_{05}}{p_0} \tag{10}$$

is the nondimensional plenum pressure, p_{05} being the total pressure in the plenum and p_0 the pressure at ambient conditions, and

$$Ma_{t,0} = \frac{U}{a_0} \tag{11}$$

is the impeller exit tip Mach number, with a_0 being the speed of sound at ambient conditions. The 1D model will be used next to simulate each of these operating conditions for comparison with experimental observations.

3.1 Deep Surge With $T_{DS} = 3.0$ s. Starting at the $T_{DS} = 3.6$ s operating point (Fig. 6), a slight decrease in throttle area reduces T_{DS} to 3.0 s with a time-averaged flow coefficient $\phi_c = 0.225$, as shown in Fig. 8. There are also four regions of flow in the 3.0 s deep surge cycle. The "quiet" region in ϕ_c occurs between points 1 and 2, where $Ma_{t,0}$ is increasing and ϕ_c is decreasing slightly as the compression system approaches the stable/mild surge boundary (stability limit). After the compressor stability limit is crossed at point 2, the compressor enters the "instability growth" phase and operates in mild surge with a frequency of approximately 7 Hz. The mild surge oscillations are also observable (to a lesser extent) in the $Ma_{t,0}$ and ψ_p traces. The mild surge fluctuations continue to grow until the beginning of the "blowdown" phase at point 3, where the flow reverses. Once again, the flow coefficient in Fig. 8 is based on the velocity measurements from the hotwire anemometer, but a corresponding plenum mass balance analysis is not provided by Fink. Since the flow is reversed during the blowdown period and the velocity measurement was transparent to the flow direction, the maximum ϕ_c during this phase (at point 4) in fact represents the minimum value. During the

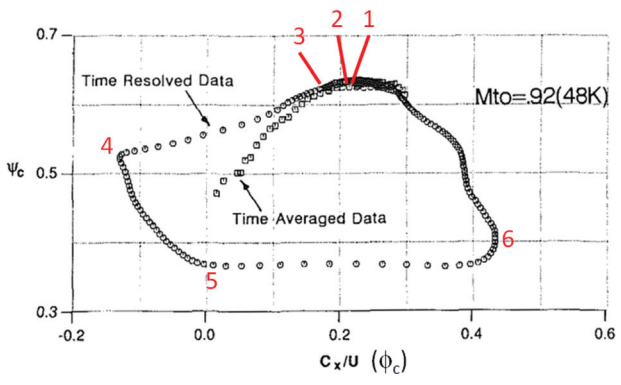

Fig. 10 Experimental time-resolved large *B* compressor data with $T_{DS} = 3.0$ s and small *B* time-averaged data of Fink et al. [3]

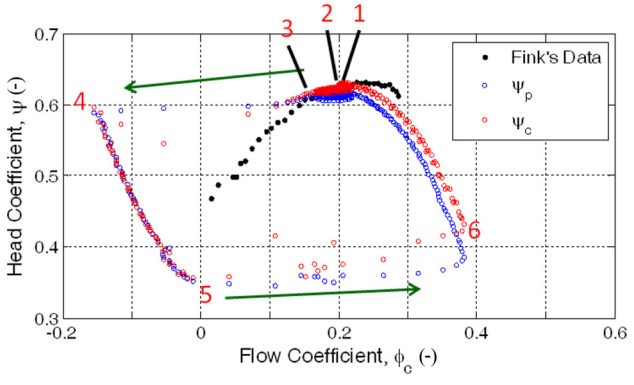

Fig. 11 Predicted time-resolved large *B* nondimensional compressor and plenum operating points with $T_{DS} = 3.0$ s along with small *B* data of Fink et al. [3]

Downloaded From: http://turbomachinery.asmedigitalcollection.asme.org/ on 05/10/2016 Terms of Use: http://www.asme.org/about-asme/terms-of-use

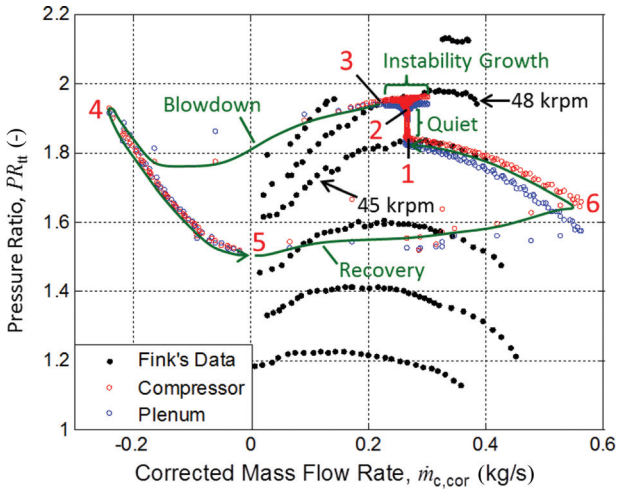

Fig. 12 Predicted time-resolved large *B* compressor and plenum operating points with $T_{DS} = 3.0$ s along with the small *B* data of Fink [2]

blowdown period, $Ma_{t,0}$ increases at a faster rate due to the lower reverse flow compressor power, and ψ_p decreases rapidly due to flow exiting the plenum through both the compressor and the throttle valve. At point 5, the flow accelerates rapidly back to the forward direction during the "recovery" period, then ϕ_c reaches a maximum value at point 6. Next, ϕ_c decreases and ψ_p increases as the operating point moves toward the quiet period (point 1) and the cycle is repeated. The corresponding simulation results from the present study are presented in Fig. 9, with the horizontal and vertical axes maintained equal to those in Fig. 8 for ease of comparison. The numbering convention used to separate the flow phases in Fig. 9 is identical to that in Fig. 8, where the numbered locations designate the boundaries between flow phases for the figure in which they appear.

A decrease in the throttle diameter by 0.12 mm (0.84% flow area reduction) is the sole difference between the predictions in Figs. 7 and 9, resulting in a decrease in T_{DS} from 3.6 to 3.0 s. The predicted nondimensional parameters in Fig. 9 compare closely with the measurements of Fink [2] in Fig. 8. The simulation contains the four phases (quiet, instability growth, blowdown, and recovery) of compressor flow coefficient behavior as observed experimentally. However, the length of the instability growth period (between points 2 and 3) and the maximum amplitude of the secondary Helmholtz resonator oscillations are smaller in predictions relative to the measurements. The predicted T_{DS} reproduces 3.0 s of the experiment. The simulated $Ma_{t,0}$ and ψ_p also appear to nearly replicate the corresponding experimental observations.

The time-resolved nondimensional compressor operating points from the experimental observations of Fink (recall Fig. 8) along

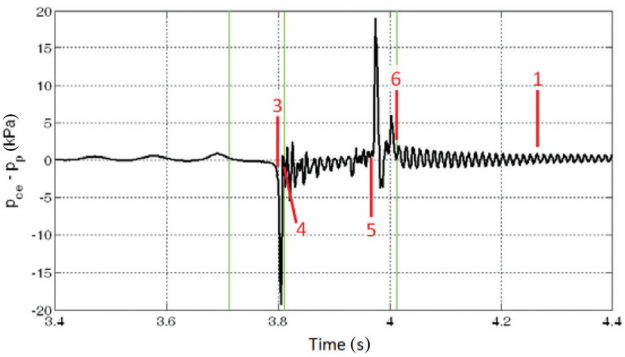

Fig. 13 Predicted p_{ce}–p_p with $T_{DS} = 3.0$ s

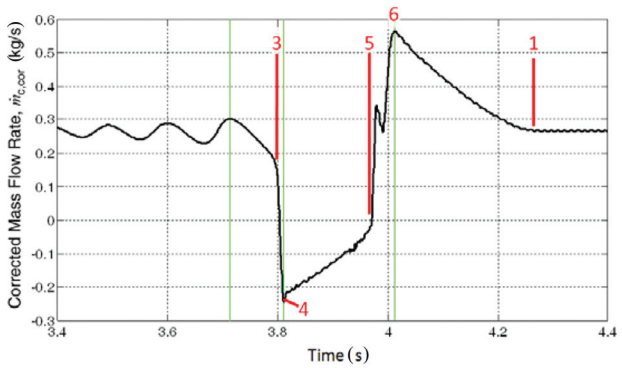

Fig. 14 Predicted, corrected compressor mass flow rate with $T_{DS} = 3.0$ s

with the time-averaged small *B* data are shown in terms of ψ_c versus ϕ_c in Fig. 10, where the numbered operating points correspond to those in Fig. 8. The compressor flow coefficient ϕ_c in Fig. 10 was estimated from the plenum mass balance. Fink used the nondimensional *plenum* pressure Π_p to estimate the nondimensional *compressor* pressure by applying the momentum balance

$$\Pi_c = \Pi_p + \frac{1}{p_0}\frac{L}{A}_C\frac{d\dot{m}_c}{dt} \tag{12}$$

to the equivalent compressor duct, in order to account for the inertia. He then used Π_c from Eq. (12) to estimate the compressor isentropic head coefficient as

$$\psi_c = \frac{\Pi_c^{(\gamma-1)/\gamma} - 1}{(\gamma - 1)Ma_{t,0}^2} \tag{13}$$

depicted in Fig. 10. The corresponding predicted operating points (recall Fig. 9) for both the compressor and plenum along with the time-averaged small *B* data of Fink are shown in Fig. 11, where the numbered operating points coincide with those in Fig. 9. The mass flow rate and pressure are spatially distributed in the predictions, allowing ϕ_c to be calculated by substituting the compressor mass flow rate in Eq. (8) and ψ_c to be calculated by substituting the nondimensional compressor pressure

$$\Pi_c = \frac{p_{03}}{p_0} \tag{14}$$

into Eq. (13), p_{03} being the total pressure at the compressor exit. The operating points in Figs. 10 and 11 have uniformly spaced time intervals of 3.2 ms, making, for example, the rate of change of ϕ_c and ψ clearly visible. During the beginning of the blowdown phase, between points 3 and 4 (3 → 4), the simulated transition from forward to reverse flow appears to occur at a faster rate than the measurement. Due to the extremely fast transitions between the forward and reverse flow characteristics (3 → 4) in Fig. 11, the predicted *plenum* head coefficient is nearly unchanged during these times. The predicted nondimensional compressor operating points in Fig. 11 agree reasonably well with the estimation from the measurements of Fink [2] in Fig. 10.

In addition, animations of the nondimensional compressor operating points in this work are available online [14], where a blue circle is utilized to depict time-resolved changes. These animations are for two complete surge cycles, but the playback speed has been reduced by a factor of ten (3.0 s surge cycle animated over 30 s) to improve the ability to visualize the deep surge phenomenon. The animations clearly demonstrate the rate at which the compressor operation moves through the different flow phases, especially for the $T_{DS} = 3.0$ s case that spends a majority of the cycle in the quiet (stable) phase near the peak head coefficient.

Downloaded From: http://turbomachinery.asmedigitalcollection.asme.org/ on 05/10/2016 Terms of Use: http://www.asme.org/about-asme/terms-of-use

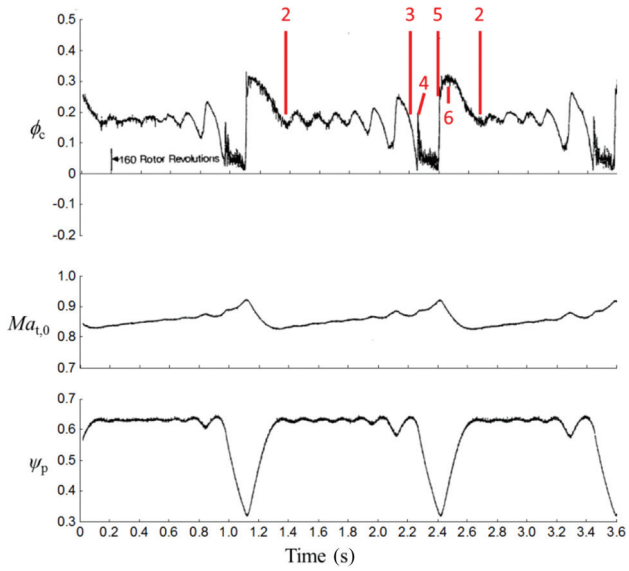

Fig. 15 Deep surge experimental data of Fink [2] with $T_{DS} = 1.24$ s

The compression system operating points in the ψ versus ϕ_c space provide a useful (collapsed) view of flow and pressure fluctuations, while the details of rotational speed oscillations become implicit. These speed fluctuations are clearly observable, however, when the deep surge cycles are viewed in the more familiar pressure ratio versus corrected mass flow rate space. Such predicted (PR_{tt} versus $\dot{m}_{c,cor}$) compressor and plenum operating points are shown in Fig. 12 along with the small B compressor characteristics of Fink. The uniform 3.2 ms interval between operating points has been maintained to make the rate of change clearly visible. A majority of the cycle is spent on the steady-state forward (6 → 2) and reverse (4 → 5) flow characteristics, while operating away from the characteristics during a portion of the instability growth phase [10] along with the fast transitions from forward to reverse flow (3 → 4) and reverse to forward flow (5 → 6).

The four phases of operation are clearly observable in Fig. 12. The quiet period (1 → 2) begins at the peak of the 45 krpm ($Ma_{t,0} = 0.86$) characteristic and continues until the rotational speed approaches 48 krpm ($Ma_{t,0} = 0.92$), which is also evident in Fig. 9. The compressor moves through this region of the deep

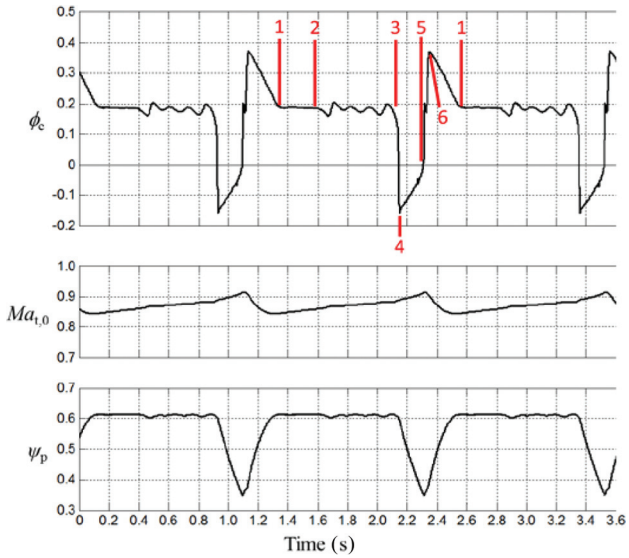

Fig. 16 Deep surge prediction with $T_{DS} = 1.22$ s

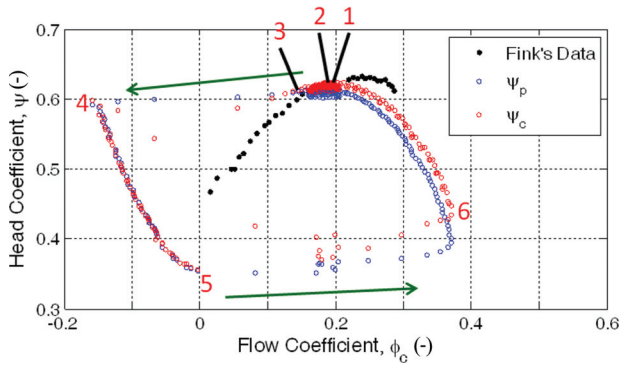

Fig. 17 Predicted time-resolved large B nondimensional compressor and plenum operating points with $T_{DS} = 1.22$ s along with small B data of Fink et al. [3]

surge cycle at a slow rate relative to the other phases. Instability growth begins at point 2 as the speed approaches 48 krpm with mild surge oscillations similar to that by Dehner et al. [10]. During the blowdown phase, the flow quickly decelerates from point 3 until it reverses and reaches a minimum value of 0.24 kg/s at point 4. As the compressor moves from points 4 to 5 along the reverse flow characteristic, the pressure ratio decreases and the flow rate increases. At point 5, the flow rate quickly transitions back to the forward direction, reaching the maximum value of 0.56 kg/s at point 6. The pressure ratio is nearly unchanged during this transition because the compressor moves through this region at a rather fast rate. At point 6, the predicted power absorbed by the compressor is nearly 47 kW, causing the rotational speed to decrease as the operating point moves toward the beginning of the quiet period (point 1). During this deep surge cycle, the predicted compressor speed fluctuates between 45.1 and 49.4 krpm with a peak-to-peak amplitude of 4.3 krpm (9.1% of the mean).

Animations of the predicted compressor operating points in the $PR_{c,tt}$ versus $\dot{m}_{c,cor}$ space are also available [14]. These animations are for two complete surge cycles, and the playback speed has been reduced by a factor of 10. For the $T_{DS} = 3.0$ s case, the relatively slow increase in rotational speed (and therefore pressure ratio) during the quiet phase is clearly visible in the animation.

The difference (p_{ce} p_p) between the predicted pressures at the compressor exit p_{ce} and in the plenum p_p, as shown in Fig. 13 (corresponding to $t = 3.4$–4.4 s in Fig. 9), represents the net pressure force acting on the air in the compressor exit duct. The green vertical lines in Figs. 13 and 14 indicate the maximum mass flow

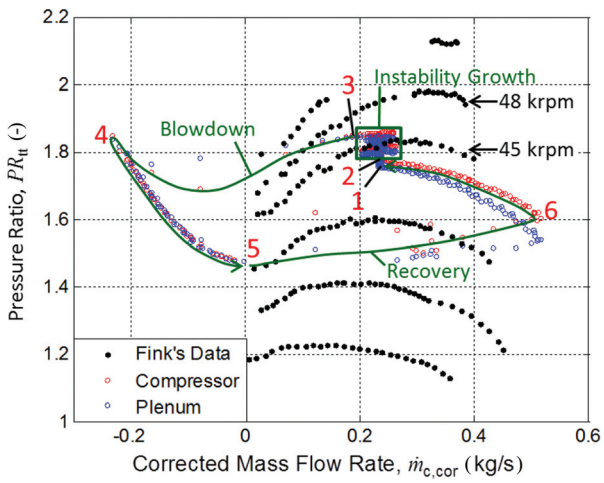

Fig. 18 Predicted time-resolved large B compressor and plenum operating points with $T_{DS} = 1.22$ s along with the small B data of Fink [2]

Downloaded From: http://turbomachinery.asmedigitalcollection.asme.org/ on 05/10/2016 Terms of Use: http://www.asme.org/about-asme/terms-of-use

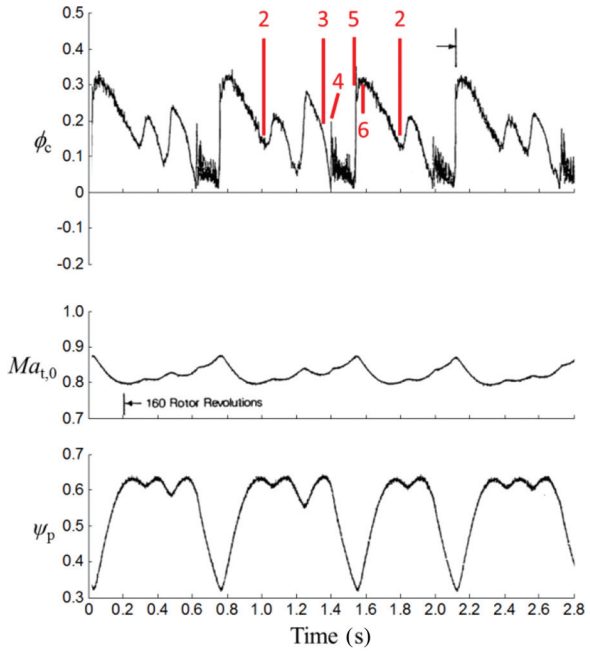

Fig. 19 Deep surge experimental data of Fink [2] with $T_{DS} = 0.70$ s

rates during the instability growth (left line) and recovery (right line) phases along with the minimum flow rate in the blowdown (middle line) period. Between points 3 and 4 in Fig. 13, the large negative spike of p_{ce}–p_p provides a (negative) force acting to decelerate the flow until it reaches the minimum value at point 4, as shown in Fig. 14. Immediately following point 5 in Fig. 14, the flow is then accelerated due to the net (positive) force created by the large (positive) spike of p_{ce}–p_p, as shown in Fig. 13.

3.2 Deep Surge With $T_{DS} = 1.24$ s. As the throttle at the exit of the compression system is further closed, the experimental observations of Fink [2] demonstrate that T_{DS} decreases from 3.0 s to approximately 1.24 s ($\phi_c = 0.19$), as shown in Fig. 15. The

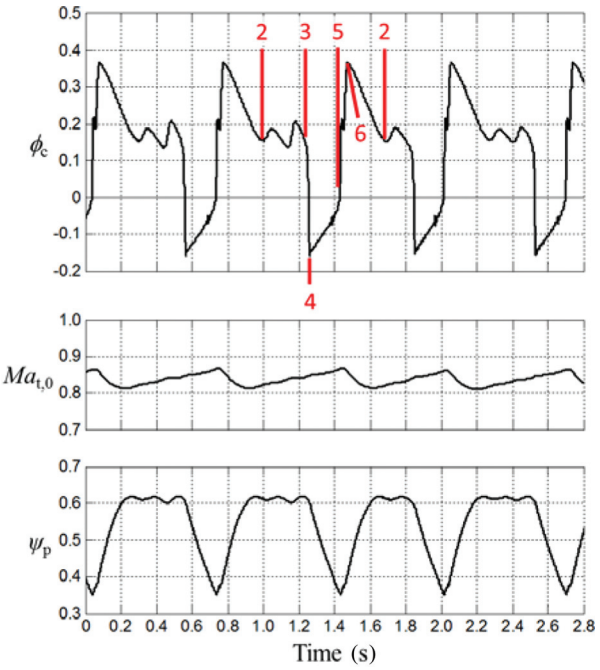

Fig. 20 Deep surge prediction with $T_{DS} = 0.68$ s

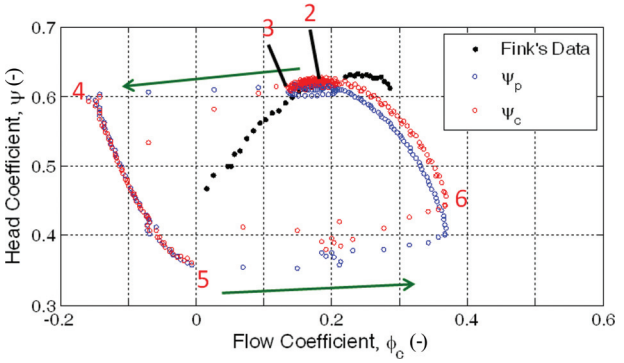

Fig. 21 Predicted time-resolved large *B* nondimensional compressor and plenum operating points with $T_{DS} = 0.68$ s along with small *B* data of Fink et al. [3]

quiet phase (1 → 2) of the deep surge cycles with $T_{DS} = 3.0$ s of Fig. 8 is now eliminated when ϕ_c is reduced experimentally from 0.225 to 0.19 of Fig. 15. During the instability growth phase in Fig. 15, the deep surge cycles undergo either 5 or 6 Helmholtz resonator cycles. The two complete deep surge cycles in Fig. 15 have periods of approximately 1.30 and 1.18 s (1.24 s being the average), with the difference roughly equal to the Helmholtz resonance period.

In the simulation, T_{DS} also decreases to 1.22 s, as shown in Fig. 16, when the throttle area is reduced by approximately 6.0%, which agrees closely with the measured 1.24 s. The predicted ϕ_c, $Ma_{t,0}$, and ψ_p appear to nearly reproduce the measurements during the dominant blowdown and recovery phases. However, a short quiet period (1 → 2) precedes the predicted instability growth phase (2 → 3), which is not observed in the measurements. The predicted amplitudes of Helmholtz resonator oscillations are also lower than the corresponding measurements. Overall, the simulation is capable of predicting the period and amplitudes during the dominant blowdown (3 → 5) and recovery (5 → 1) portions of the deep surge cycles with reasonable accuracy. In Figs. 16–18, the same numbering convention is used for the predicted compressor operating points, allowing the phases of flow to be observed in different spaces.

The predicted compressor and plenum nondimensional operating points with a deep surge cycle period of 1.22 s are shown in Fig. 17 and the corresponding animation [14], which are very similar to those of the 3.0 s period in Fig. 11. Decreasing the throttle diameter also reduces the time-averaged ϕ_c during the instability growth phase, as shown by comparison of point 2 in Figs. 11 and

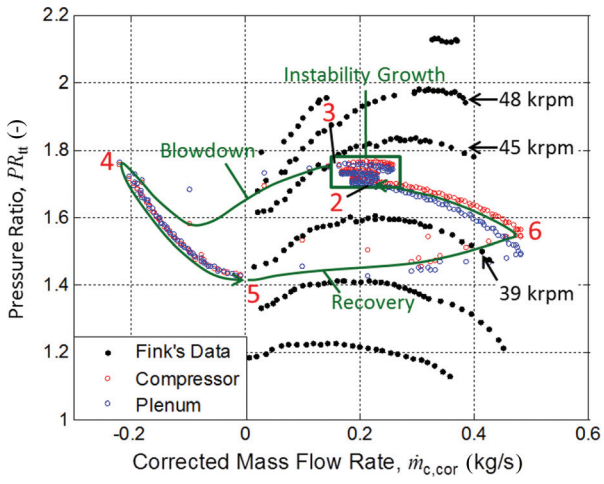

Fig. 22 Predicted time-resolved large *B* compressor and plenum operating points with $T_{DS} = 0.68$ s along with the small *B* data of Fink [2]

Downloaded From: http://turbomachinery.asmedigitalcollection.asme.org/ on 05/10/2016 Terms of Use: http://www.asme.org/about-asme/terms-of-use

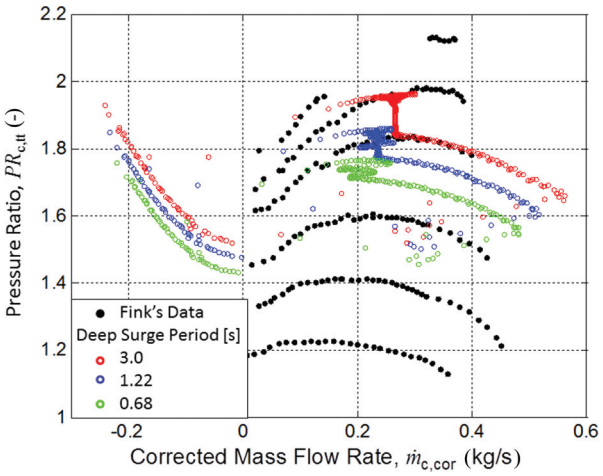

Fig. 23 Predicted time-resolved large *B* compressor operating points with $T_{DS} = 3.0$, 1.22, and 0.68 s along with small *B* data of Fink [2]

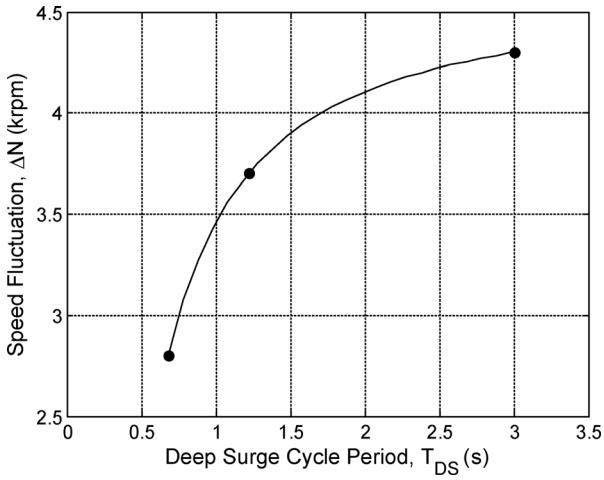

Fig. 25 Peak-to-peak amplitude of rotational speed fluctuations as a function of T_{DS}

17. This trend is consistent with the corresponding observations of Fink [2], where ϕ_c decreased from 0.225 to 0.19 with a reduction in the throttle flow area.

The predicted (PR_{tt} versus $\dot{m}_{c,cor}$) compressor and plenum operating points along with the small *B* compressor characteristics of Fink are shown in Fig. 18 and the corresponding animation [14]. Once again, a majority of the cycle is spent on the steady-state forward (6 →←2) and reverse (4 →←5) flow characteristics. The compressor operates away from the characteristics during a portion of the instability growth phase (2 →←3) and the small fraction of time required to transition from forward to reverse flow (3 → 4) and reverse to forward flow (5 → 6). The four phases of operation are clearly observable in Fig. 18. The quiet period (1 → 2) of the 1.22 s deep surge cycle is shorter in duration and occurs at lower pressure ratios and rotational speeds than that of the 3.0 s period in Fig. 12. Instability growth begins (point 2) as the speed approaches 45 krpm and continues until it reaches 46 krpm (point 3). Next, the flow quickly reverses in the blowdown phase until it reaches a minimum value of 0.23 kg/s at point 4. As the compressor operating point moves along the reverse flow characteristic to point 5, the pressure ratio decreases and the flow rate increases. Then, the flow rate quickly transitions back to the forward direction, reaching the maximum value of 0.52 kg/s at point 6. At point 6, the predicted power absorbed by the compressor is nearly 41 kW, causing the rotational speed to decrease as the operating point moves toward the beginning of the quiet period (point 1). The predicted compressor speed fluctuates between 43.9 and 47.5 krpm with a peak-to-peak amplitude of 3.7 krpm (8.1% of the mean).

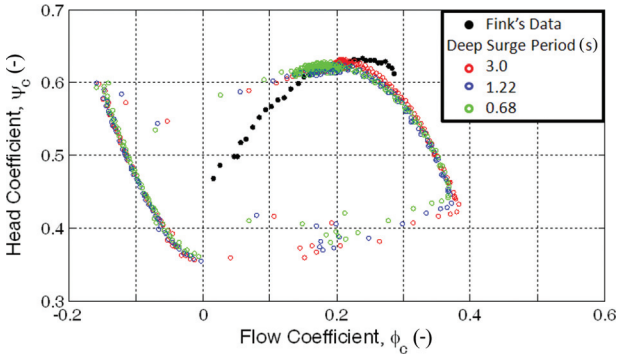

Fig. 24 Predicted time-resolved large *B* compressor nondimensional operating points with $T_{DS} = 3.0$, 1.22, and 0.68 s along with small *B* data of Fink et al. [3]

3.3 Deep Surge With $T_{DS} = 0.70$ s. Experimental observations of Fink [2] demonstrated that an even further decrease in throttle area reduced T_{DS} to approximately 0.70 s ($\phi_c = 0.16$), as shown in Fig. 19. The number of Helmholtz resonator periods during the instability growth phase is one or two (varies cycle-to-cycle). Starting at the predicted $T_{DS} = 1.22$ s case of Sec. 3.2, an 8.2% reduction in throttle area is accompanied by a decrease to $T_{DS} = 0.68$ s, as shown in Fig. 20, which agrees closely with the measurement. A quiet period does not occur in the prediction or the measurement, as shown in Figs. 19 and 20. The simulated number of Helmholtz resonator oscillations, during the instability growth period, is one or two, which reproduces the experimental observation of Fink [2], while the predicted amplitudes of the Helmholtz resonator oscillations are lower than the corresponding measurements. Overall, the simulation is capable of predicting the deep surge cycles with reasonable accuracy.

The predicted compressor and plenum nondimensional operating points with $T_{DS} = 0.68$ s are shown in Fig. 21 and the

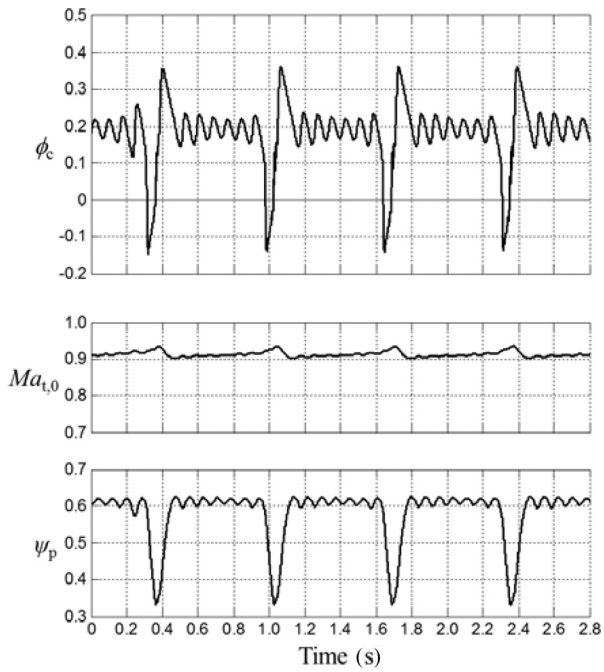

Fig. 26 Elimination of the quiet phase from the $T_{DS} = 3.0$ s period by reducing *B* from 2.74 to 1.37

Downloaded From: http://turbomachinery.asmedigitalcollection.asme.org/ on 05/10/2016 Terms of Use: http://www.asme.org/about-asme/terms-of-use

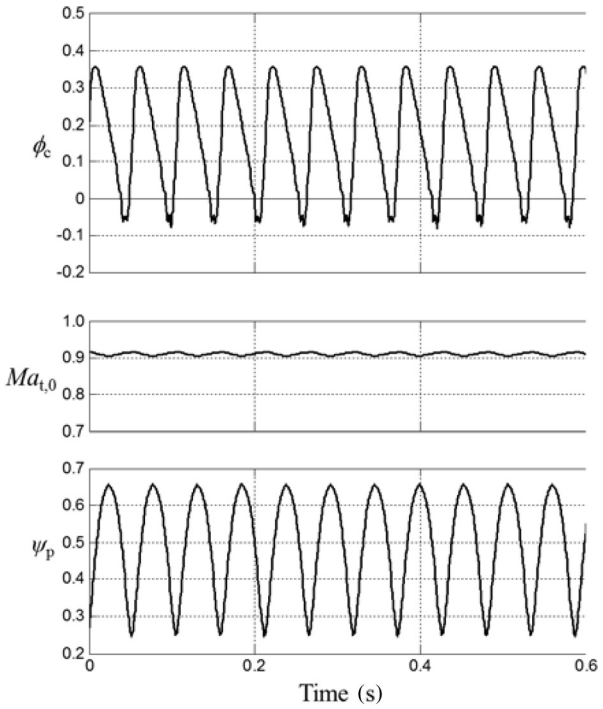

Fig. 27 Elimination of both the quiet and instability growth phases from the $T_{DS} = 3.0$ s period by reducing B from 2.74 to 0.53

corresponding animation [14], which are very similar to those with $T_{DS} = 3.0$ and 1.22 s periods in Figs. 11 and 17, respectively. Figures 20–22 use the same numbering convention for the predicted compressor operating points, allowing the phases of flow to be observed in different spaces.

The predicted (PR_{tt} versus $\dot{m}_{c,cor}$) compressor and plenum operating points are shown in Fig. 22 and the corresponding animation [14], along with the small B compressor characteristics of Fink. The instability growth, blowdown, and recovery phases of operation are clearly observable in Fig. 22, while the quiet period is eliminated.

Once again, majority of the cycle is spent on the steady-state forward (6 → 2) and reverse (4 → 5) flow characteristics, while operating away from the characteristics during a portion of the instability growth phase (2 → 3) along with the small fractions of time required to transition from forward to reverse flow (3 → 4) and reverse to forward flow (5 → 6). Instability growth begins (point 2) as the speed approaches 42.6 krpm and continues until the speed reaches 43.8 krpm at point 3. Next, the flow quickly reverses in the blowdown phase until it reaches a minimum value of 0.21 kg/s at point 4. As the compressor operating point moves along the reverse flow characteristic to point 5, the pressure ratio decreases and the flow rate increases. Then, the flow quickly transitions back to the forward direction, reaching the maximum value of 0.48 kg/s at point 6. At point 6, the predicted power absorbed by the compressor is nearly 35 kW, causing the rotational speed to decrease as the operating point moves toward the beginning of the instability growth period (point 2). The predicted compressor speed fluctuates between 42.2 and 45.0 krpm with a peak-to-peak amplitude of 2.8 krpm (6.4% of the mean).

3.4 Additional Observations. When the deep surge cycles are viewed in the $PR_{c,tt}$ versus $\dot{m}_{c,cor}$ plane, the time-resolved "surge loops" are noticeably different for each operating point, as shown in Fig. 23. A decrease in the throttle diameter shifts the pressure ratios and rotational speeds to lower values. Furthermore, the maximum $\dot{m}_{c,cor}$ decreases and the minimum increases slightly as the duration of the deep surge cycle is reduced. It is interesting to note that, despite these differences in the $PR_{c,tt}$ versus $\dot{m}_{c,cor}$ plane, the time-resolved surge loops in the nondimensional ψ_c versus ϕ_c plane are nearly identical for all three deep surge predictions, as illustrated in Fig. 24.

The quiet and instability growth phases exhibited by Fink's compression system have not been observed during deep surge cycles in numerous other studies [5–7,12,13,15,16]. Fink's rather large plenum (208 L) required substantial periods of time to empty and fill during the blowdown and recovery flow phases. During a portion (4 → 5) of the blowdown phase, the compressor operates on the reverse flow characteristic while the plenum pressure decreases. The compressor consumes little power in this operating region, causing the rotational speed to increase. When the flow recovers back to the forward direction, the compressor must operate at high mass flow rates while the plenum pressure increases. Here, the compressor consumes a significant amount of power, resulting in a large reduction in speed. This unusually large speed reduction is responsible for the occurrence of the quiet and instability growth flow phases, as will be illustrated next.

During the recovery phase of the predicted $T_{DS} = 3.0$ s deep surge cycle (recall Fig. 12), the compressor rotational speed decreases by approximately 4 krpm. At the end of the recovery phase (point 1), the speed is nearly 3 krpm below that at the onset of instability growth (point 2), allowing the compression system to operate in a stable mode as the speed increases at a relatively slow rate. As the throttle flow rate of the $T_{DS} = 3.0$ s case was reduced computationally, the quiet phase was nearly eliminated from the deep surge cycles, therefore decreasing T_{DS} to 1.22 s. The quiet period is nearly eliminated due to the lower amplitude of rotational speed fluctuations ΔN of the $T_{DS} = 1.22$ s case relative to that when $T_{DS} = 3.0$ s, as shown in Fig. 25. The smaller ΔN places the compressor operating point closer to the stability limit (point 2) of the system at the end of the recovery phase (point 1). The quiet phase is eliminated and the duration of the instability growth phase decreases when T_{DS} is further reduced to 0.68 s, due to the significantly lower ΔN for this case.

4 Occurrence of Quiet and Instability Growth Flow Phases

In order to illustrate the influence of plenum volume on ΔN (and therefore the occurrence of the quiet and instability growth phases), the plenum volume of the $T_{DS} = 3.0$ s deep surge cycle was reduced computationally. When the plenum volume is reduced from 208 to 52 L (B from 2.74 to 1.37), the quiet phase is eliminated, as shown in Fig. 26 (contrast with Fig. 9). The reduction in volume is accompanied by a decrease in ΔN from 4.3 to 1.66 krpm. A further reduction of plenum volume to 7.9 L (B to 0.53) eliminates both the quiet and instability growth phases, as shown in Fig. 27. This larger volume reduction decreases ΔN to 0.52 krpm. The deep surge cycles in Fig. 27 are comprised of only blowdown and recovery phases, which may be more typical for reasonably sized plenum volumes in vehicle applications.

The computations also illustrate that the quiet and instability growth deep surge cycle flow phases disappear when the rotational inertia is increased to a rather large value (ΔN is decreased), which is consistent with the conclusion that large speed fluctuations contribute to the occurrence of these phases.

5 Conclusions

The current study demonstrated the ability to predict centrifugal compression system deep surge physics using a 1D time domain engine simulation code. A number of significant modifications were incorporated into the code to improve the compressor characterization, including low and reverse flow performance, reverse flow compressor power, and compressor equivalent geometry. Prediction results from the present 1D model improve agreement with experimental data relative to previous 0D models, due to elimination of many of the simplifying assumptions.

Downloaded From: http://turbomachinery.asmedigitalcollection.asme.org/ on 05/10/2016 Terms of Use: http://www.asme.org/about-asme/terms-of-use

The deep surge simulations from the present study captured the distinct flow phases evident in the experimental results of Fink. In addition, the predicted deep surge cycle periods along with the dominant amplitudes during the blowdown and recovery phases, showed good agreement with measurements. During the instability growth phase, the deep surge predictions slightly underestimated the amplitudes of fluctuations, while the frequency and number of Helmholtz resonator oscillations provided reasonable agreement with measurements. All of the predicted deep surge cycles are nearly identical in the ψ_c versus ϕ_c space, while noticeable differences are observed in the PR_c versus $\dot{m}_{c,cor}$ space.

In order to demonstrate that the unusual quiet and instability growth flow phases result from large amplitude speed fluctuations, computational simulations from the present study were also completed with a substantially reduced plenum volume and increased rotational inertia.

Nomenclature

a = speed of sound
A = cross-sectional area
B = nondimensional Greitzer number
C_x = axial velocity
f_H = Helmholtz resonator frequency
L, l = length
$\dot{m}$ = mass flow rate
$Ma_{t,0}$ = Mach number of impeller tip
N = turbocharger shaft rotational speed
p = pressure
P = power
PR = pressure ratio
t = time
T = temperature
T_{DS} = period of deep surge cycle
U = velocity of the impeller tip
V = volume

Greek Symbols

γ = ratio of specific heats
Δ = change in parameter
η = isentropic efficiency
Π = nondimensional pressure
ρ = density
ϕ = flow coefficient
ψ = isentropic head coefficient

Subscripts

c = compressor
C = equivalent compressor duct
ce = compressor exit
cor = corrected
p = plenum
ref = reference
ts = total-to-static
tt = total-to-total
0 = ambient; total property
1 8 = location

References

[1] Cumpsty, N. A., 1989, *Compressor Aerodynamics*, Krieger, Malabar, FL.
[2] Fink, D. A., 1988, "Surge Dynamics and Unsteady Flow Phenomena in Centrifugal Compressors," Ph.D. thesis, Department of Aeronautics and Astronautics, Massachusetts Institute of Technology, Cambridge, MA.
[3] Fink, D. A., Cumpsty, N. A., and Greitzer, E. M., 1992, "Surge Dynamics in a Free-Spool Centrifugal Compressor System," ASME J. Turbomach., **114**(2), pp. 321–332.
[4] Greitzer, E. M., 1976, "Surge and Rotating Stall in Axial Flow Compressors, Part I: Theoretical Compression System Model," ASME J. Eng. Power, **98**(2), pp. 190–197.
[5] Yano, T., and Nagata, B., 1971, "A Study on Surging Phenomena in Diesel Engine Air-Charging System," Jpn. Soc. Mech. Eng., **14**(70), pp. 364–376.
[6] Greitzer, E. M., 1976, "Surge and Rotating Stall in Axial Flow Compressors, Part II: Experimental Results and Comparison With Theory," ASME J. Eng. Power, **98**(2), pp. 199–217.
[7] Uhlenhake, G., Selamet, A., Fogarty, K., Tallio, K., and Keller, P., 2011, "Development of an Experimental Facility to Characterize Performance, Surge, and Acoustics in Turbochargers," SAE Paper No. 2011-01-1644.
[8] Hansen, K. E., Jorgensen, P., and Larsen, P. S., 1981, "Experimental and Theoretical Study of Surge in a Small Centrifugal Compressor," ASME J. Fluids Eng., **103**(3), pp. 391–395.
[9] Theotokatos, G., and Kyrtatos, N. P., 2001, "Diesel Engine Transient Operation With Turbocharger Compressor Surging," SAE Paper No. 2001-01-1241.
[10] Dehner, R., Selamet, A., Keller, P., and Becker, M., 2010, "Simulation of Mild Surge in a Turbocharger Compression System," SAE J. Engines, **3**(2), pp. 197–212.
[11] Gamma Technologies, 2009, "GT-Power (Version 7.0)," Gamma Technologies, Westmont, IL.
[12] Dehner, R., Selamet, A., Keller, P., and Becker, M., 2011, "Prediction of Surge in a Turbocharger Compression System vs. Measurements," SAE J. Engines, **4**(2), pp. 2181–2192.
[13] Dehner, R., 2011, "Simulation of Surge in Turbocharger Compression Systems," M.S. thesis, Department of Mechanical Engineering, The Ohio State University, Columbus, OH.
[14] Selamet, A., 2016, "Deep Surge Animations," http://engine.osu.edu
[15] Galindo, J., Serrano, J. R., Climent, H., and Tiseria, A., 2008, "Experiments and Modeling of Surge in Small Centrifugal Compressor for Automotive Engines," Exp. Therm. Fluid Sci., **32**(3), pp. 818–826.
[16] Emmons, H. W., Pearson, C. E., and Grant, H. P., 1955, "Compressor Surge and Stall Propagation," Trans. ASME, **77**(4), pp. 455–469.

Downloaded From: http://turbomachinery.asmedigitalcollection.asme.org/ on 05/10/2016 Terms of Use: http://www.asme.org/about-asme/terms-of-use